Space charge effects on the third order coupled resonance

Giuliano Franchetti,[1,2] Simone Gilardoni,[3] Alexander Huschauer,[3]
Frank Schmidt,[3] and Raymond Wasef[2,3]

[1]GSI Helmholtzzentrum für Schwerionenforschung GmbH, 64291 Darmstadt, Germany
[2]Goethe University Frankfurt, Max-von-Laue-Straße 7, 60438 Frankfurt am Main, Germany
[3]CERN, CH 1211 Geneva 23, Switzerland

(Received 28 January 2017; published 31 August 2017)

The effect of space charge on bunched beams has been the subject of numerous numerical and experimental studies in the first decade of 2000. Experimental campaigns performed at the CERN Proton Synchrotron in 2002 and at the GSI SIS18 in 2008 confirmed the existence of an underlying mechanism in the beam dynamics of periodic resonance crossing induced by the synchrotron motion and space charge. In this article we present an extension of the previous studies to describe the effect of space charge on a controlled coupled (2D) third order resonance. The experimental and simulation results of this latest campaign shed a new light on the difficulties of the 2D particle dynamics. We find striking experimental evidence that space charge and the coupled resonance create an unusual coupling in the phase space, leading to the formation of an asymmetric halo. Moreover, this study demonstrates a clear link between halo formation and fixed-lines.

DOI: 10.1103/PhysRevAccelBeams.20.081006

I. INTRODUCTION

The effect of space charge in a bunched beam stored for a time scale of one second has been the subject of two experimental campaigns, the first at CERN [1], and the second at GSI [2]. The necessity of those experiments was motivated by new operational regimes required by the FAIR project [3], and also by the recent interest of CERN in using high brightness beams as part of the LIU project [4]. This unprecedented mode of operation in synchrotrons leads to the interaction of space charge with lattice nonlinearities for large number of machine turns. A lot of experience in non-linear dynamics has been gained from projects with colliders and storage rings, in particular for the LHC (see references in [5]). Also space charge dominated beams have been studied in-depth [6]. The accelerator operations experience in this hybrid scientific regime is, however, a matter of further investigation.

The understanding of the key ingredients for operating an accelerator in this regime poses a number of challenges. First, it is conceptually difficult to describe beam loss and emittance growth mechanisms. Second, one faces problems in developing adequate computational models that will be valid despite their unavoidable approximations. Last, for the understanding of the complex beam dynamics, and the development and validation of the code modeling, an experimental verification is required: initially at a qualitative level, in order to confirm the basic mechanism, and subsequently via simulation codes to verify their predictive power.

At the numerical level, past studies have primarily addressed the understanding of the effect of the space charge on a single 1D resonance ($nQ_x = p$). This choice allowed a visualization of the dynamics in terms of Poincaré surfaces of section, which in this case is two dimensional, making the discussion of the basic mechanisms easier to understand.

The first experiment at the CERN Proton Synchrotron (PS) [1] showed that a slow emittance growth takes place during the time of storage, when the space charge tune-spread overlaps an artificially excited 4th order resonance. An overall emittance growth of ~80% after a storage time of one second, was reported. The slow emittance growth was attributed to the process of periodic resonance crossing driven by the longitudinal motion of particles along the bunch in combination with space charge induced detuning. The experiment was modelled with a simplified lattice, and the simulation results have approximately reproduced the emittance growth. The numerical studies have also excluded a significant contribution of coherent resonances. In fact, it was found that the coherent effects of space charge [7–9] are significantly Landau damped by the nonlinear detuning from space charge itself [10]. This has allowed to limit the modelling to the incoherent effects of space charge only. These frozen models have been applied in similar studies of single crossing of one resonance [11,12]. The conclusion of the first experimental campaign was that the experiment itself could not demonstrate the existence of the beam physics mechanism invoked.

This point was readdressed later by an experimental campaign at GSI [2], where two beams, one bunched and

Published by the American Physical Society under the terms of the Creative Commons Attribution 4.0 International license. Further distribution of this work must maintain attribution to the author(s) and the published article's title, journal citation, and DOI.

the other one coasting, with equivalent space charge tune spreads were studied. The large emittance growth (after one second of storage time) was found for high intensity and bunched beams only. The experiment also showed that nonlinear effects from the rf system did not cause sizeable emittance growth. This experiment suffered from the fact that one had to develop an approximate model for the nonlinear errors exciting the natural $3Q_x$ (1D) resonance under scrutiny.

In this article we report the outcome of a joint CERN-GSI experimental campaign conducted at the PS, to investigate the effect of space charge on a coupled, i.e., 2D, 3rd order resonance. The motivation for this effort was two-fold: (i) the necessity of understanding and studying mitigation strategies for the SIS100 injection scenario with U^{+28} ions; and (ii) the LIU project requiring the control of high brightness beams. The complication is that one cannot find a trivial extension from 1D to 2D, even the presentation in terms of four dimensional Poincaré surfaces of section is visually demanding. In fact, a fresh theoretical analysis was required to highlight and deepen our understanding of the various aspects of 2D resonance structures [13,14].

We present the details about the experimental conditions and discuss the methodology of the data treatment and the associated simulations. This experiment has highlighted a beam response pattern completely different from previous observations, emphasizing the role of the coupled nonlinear dynamics, chromaticity, and space charge on halo formation and beam core growth. The main experimental highlight is the study of fixed-lines, and their interaction with space charge. While in terms of single particle dynamics, the theory of the fixed-lines is fully developed [13–22], the interplay of these exotic objects with space charge remains a subject of further study. Nevertheless, we will address some aspects of the role of the fixed-lines in creating the observed beam response.

The paper is structured in the following way: Sec. II describes the experimental campaign and Sec. III its results. In Sec. IV we discuss the simulation modeling and code benchmarking, followed by a discussion of the results in Sec. V. Section VI discusses the experimental results as a consequence of the presence of fixed-lines. The conclusion and an outlook are presented in Sec. VII. The Appendices A and B provide details about the PS and the treatment of the experimental data. Appendix C discusses the mathematical aspects for characterizing the overlapping of the space charge tune-spread with the resonance.

II. THE MEASUREMENT CAMPAIGN

The purpose of the experimental campaign was to study the interplay between space charge and coupled 3rd order resonances. Therefore, an appropriate resonance providing sufficient separation from other excited resonances had to be chosen. The resonances naturally excited in the PS were extensively studied in [23], where strong excitation of the skew sextupolar resonance $2Q_x + Q_y = 19$ was reported. Figure 1 shows a measured tune diagram at 2 GeV kinetic energy, where the presence of several other, but weaker, resonance lines is highlighted as well. Furthermore, the normal sextupolar resonance $Q_x + 2Q_y = 19$ appears to be only weakly excited and sufficient free space to accommodate the space charge tune spread is available in its vicinity. Based on these considerations, as well as on the fact that the resonance can be excited in a controlled way by two sextupoles installed in the straight section (SS) 39 of the PS ring, this resonance was selected for the study presented in this article. Further information about the PS can be found in Appendix A. As the strength of the line $Q_x + 2Q_y = 19$ appears to weaken close to the horizontal integer resonance, a vertical tune of $Q_y = 6.47$ in combination with horizontal

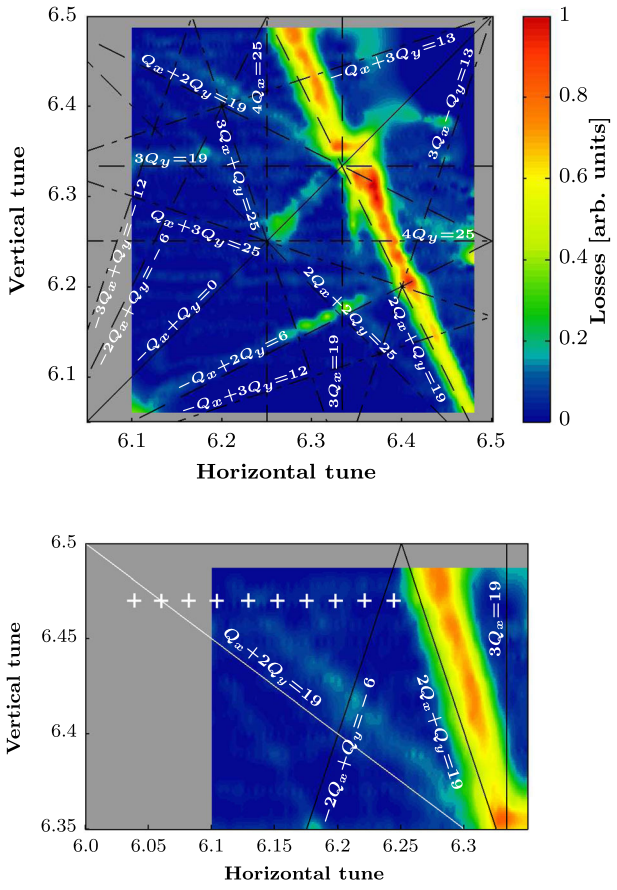

FIG. 1. Top: Experimental tune scan at 2 GeV kinetic energy. The color scale is proportional to the measured normalized beam loss. The red color indicates maximum beam loss. Solid lines indicate 2nd order, dashed lines 3rd order, and dash-dotted lines 4th order resonances. The resonance $2Q_x + Q_y = 19$ was found to be strongly excited by natural nonlinear errors of the machine. Grey areas indicate the absence of measurement data [23]. Bottom: Detail of the tune diagram shown in Fig. 1, with identical colour scale. The sextupolar resonance $Q_x + 2Q_y = 19$ is shown with a white solid line and the working points used for the systematic study are indicated with the white crosses.

TABLE I. Measured transverse tunes for the working points used in the measurement campaign. The average value resulting from three independent measurements is shown. The vertical tune is slightly shifted with respect to the constant programmed value. Δ_{r0} corresponds to the distance of the resonance as defined in Eq. (1).

Q_{x0}	Q_{y0}	Δ_{r0}	Q_{x0}	Q_{y0}	Δ_{r0}
6.039	6.479	−0.003	6.152	6.469	0.090
6.060	6.478	0.016	6.175	6.468	0.111
6.082	6.477	0.036	6.198	6.467	0.132
6.104	6.476	0.056	6.221	6.466	0.153
6.129	6.470	0.069	6.244	6.465	0.174

tunes Q_x extending from 6.0 to 6.2 were chosen to conduct the experiment. Moreover, this was motivated by the goal of staying as far as possible from the resonance $3Q_y = 19$, which is also excited by the machine errors.

As a first step during the experimental study, the resonance was weakly excited by powering the sextupoles with a current of $I_{\mathrm{SX}} \approx 2$ A, corresponding to an integrated sextupolar strength of $K_2 = 0.0149$ m^{-2} for each of them. This integrated strength is comparable to that of the natural errors in the injection scenario for SIS100, where a significant space charge tune spread will overlap with a sextupolar resonance of the type $Q_x + 2Q_y = N$.

In order to obtain a space charge tune spread exceeding the resonance stop band, but remaining small enough to avoid any overlap with the integer resonance $Q_x = 6.0$ for all working points under consideration, the bunch intensity was carefully adjusted. The ten working points selected for this study are indicated by the white crosses in the bottom plot of Fig. 1. The working points were chosen in this specific way to vary the overlap between the tune spread and the resonance. Since this study depends critically on a precise knowledge of the machine tunes Q_{x0}, Q_{y0}, the values were measured applying the base band tune measurement technique (BBQ) [24] and the results are summarized in Table I. Moreover, a list of relevant beam and accelerator parameters is presented in Table II.

TABLE II. Beam and machine parameters.

Parameter	Value
Intensity N_p [10^{10} p]	55
Normalized horizontal rms emittance ε_x^n [mm mrad]	3.6
Normalized vertical rms emittance ε_y^n [mm mrad]	2.2
Bunch length σ_t [ns]	33
Momentum spread $\frac{\Delta p}{p}$ [10^{-3}]	0.95
Horizontal maximum tune spread $\Delta Q_{x,\max}$ [a]	−0.05
Vertical maximum tune spread $\Delta Q_{y,\max}$ [a]	−0.07
Sextupole current I_{SX} [A]	2
Harmonic number h	8
Rf voltage V_{rf} [kV]	20.5
Natural horizontal chromaticity Q_x'	−5.30
Natural vertical chromaticity Q_y'	−7.02
Kinetic energy of the stored beam [GeV]	2
Number of stored turns	497646
Storage time [s]	1.1
Relativistic β	0.948
Relativistic γ	3.14
Synchrotron period [turns]	1164
β_x at the horizontal wire scanner in SS68 [m]	12.40
β_y at the vertical wire scanner in SS64 [m]	21.75

[a]The tune spread is calculated according to Ref. [25].

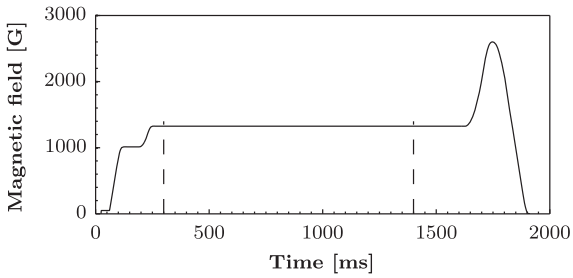

FIG. 2. Magnetic cycle of the PS as used for the measurements. The first plateau starting at 170 ms corresponds to injection kinetic energy at 1.4 GeV and the long plateau starting at 250 ms to 2 GeV. For each working point the evolution of the transverse profiles was recorded between 300 ms and 1400 ms as indicated by the dashed lines. The final acceleration is required to extract the beam towards the beam dump.

The measurements were conducted on a plateau of 2 GeV kinetic energy, where the beam was stored for 1.1 s. In order to characterize the transverse beam profiles, measurements with the horizontal and vertical wire scanners [26], located in SS68 and SS64, respectively, were recorded at the beginning and at the end of the plateau (see Fig. 2). Furthermore, the beam intensity was recorded using a beam current transformer [27] and the longitudinal phase space was reconstructed applying the tomography technique [28]. In order to compare the different profiles and to gain statistical significance, each measurement was repeated three times.

III. EXPERIMENTAL RESULTS

The interaction between the beam and the 3rd order coupled resonance was evaluated based on the measured transverse profiles, and the emittance growth between the initial and final measurements ($t_i = 300$ ms and $t_f = 1400$ ms, respectively) was chosen as a figure of merit.

As set forth in Appendix B, the rms size σ, which corresponds to either the horizontal or the vertical plane of the profiles, was determined at the two time settings along the measurement plateau. Subsequently, the ratio σ_f^2/σ_i^2 was computed, which is equal to the rms emittance growth ϵ_f/ϵ_i in the vertical plane. This ratio takes a different meaning when resonant phenomena alter the usual phase space topology, as may happen in the case of halo formation. Nevertheless, in this article we will refer to σ_f^2/σ_i^2 as the emittance growth in each plane.

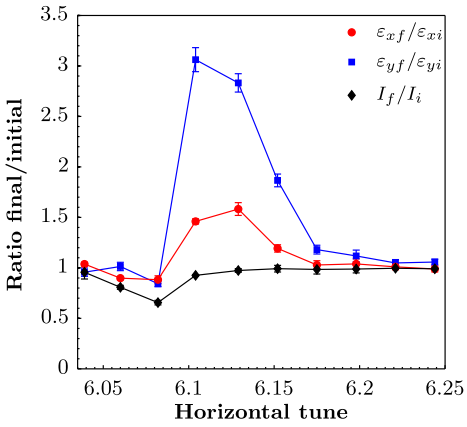

FIG. 3. Measured emittance growth and beam intensity as a function of the horizontal tune. Error bars are obtained from the statistical fluctuation resulting from three consecutive measurements.

The transverse emittance growth as well as the beam survival, i.e., the ratio between final and initial intensity I_f/I_i, as a function of the measured horizontal tunes is shown in Fig. 3. The pattern of the emittance increase is similar to the one obtained in previous experiments [1,2], and only occurs once the space charge tune spread overlaps with the resonance.

In contrast to one dimensional resonances the distance from the resonance for the machine tunes Q_{x0}, Q_{y0} is defined as

$$\Delta_{r0} = Q_{x0} + 2Q_{y0} - 19, \tag{1}$$

and the derivation and related discussion can be found in [14–16,19–21]. For the working points chosen in the experiment the distances of the resonance Δ_{r0} are reported in Table I. The condition of overlapping of the third order resonance with the space charge tune-spread of the full bunch is

$$0 \le \Delta_{r0} \le -\mathcal{D}_{\mathrm{r,sc}}, \tag{2}$$

with $\mathcal{D}_{\mathrm{r,sc}} = \Delta Q_{x,\max} + 2\Delta Q_{y,\max}$. (see in Appendix C for the derivation.)

For the space charge tune-shifts shown in Table II we find $\mathcal{D}_{\mathrm{r,sc}} = -0.19$. The left equality in Eq. (2) is obtained for $\Delta_{r0} = 0$ and yields one of the two extremes of the tune-spread overlapping: for our tune scan, at the tune $Q_{x0} = 6.06$ the space charge tune-spread is overlapping with the resonance since $\Delta_{r0} = 0.016$, while at $Q_{x0} = 6.039$ it does not overlap as $\Delta_{r0} = -0.003$. This is approximately confirmed by Fig. 3 as neither beam loss nor emittance growth is found at $Q_{x0} = 6.039$.

The larger Δ_{r0} is to the resonance, the more the machine tunes are off the resonance, and at some point the equality on the right side of Eq. (2) will be satisfied. This situation corresponds to an overlap of particles with the resonance, which experience the maximum space charge detuning. In the experiment this condition was never reached. In fact,

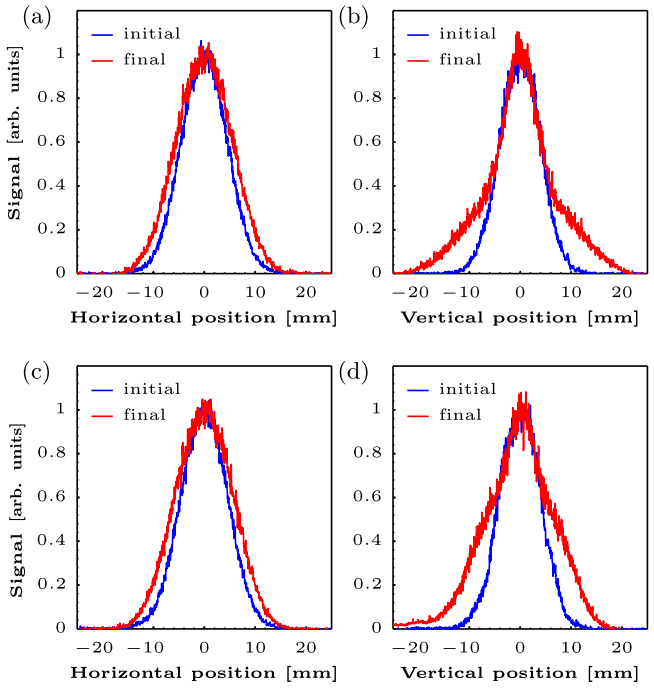

FIG. 4. Comparison between final and initial profiles at $Q_{x0} = 6.104$ for the horizontal (a) and the vertical plane (b). Figures (c) and (d) show the corresponding pictures for $Q_{x0} = 6.129$.

a horizontal tune $Q_{x0} > 6.265$ would have been required to avoid any overlap with the resonance (i.e., $\Delta_{r0} > -\mathcal{D}_{\mathrm{r,sc}}$). However, this would have caused the working point to be set inside the large stop band of the neighboring skew resonance $2Q_x + Q_y = 19$ shown in the bottom of Fig. 1. Figure 3 shows a large difference in the emittance growth between the horizontal and the vertical plane. The growth is most important at $Q_{x0} = 6.104$ and $Q_{x0} = 6.129$ with a maximum growth exceeding a factor of three: such a large value has never been observed in previous measurements. In order to visualize the situation the beam profiles for these working points are shown in Fig. 4. In both cases the horizontal and vertical profiles were found to be very different. While the horizontal profiles exhibit mainly core growth, creation of large tails in the vertical plane was observed. Moreover, a significant change of the vertical profiles is observed between the two working points. The evolution of the vertical profiles is very sensitive to minor changes of the settings of the order of $\delta\Delta_{r0} = 0.013$.

An explanation of these features as well as of the asymmetry between the transverse profiles requires a discussion on the machine induced detuning and on the effect of the 3rd order resonance. Both topics are addressed in the next sections.

IV. SIMULATION MODELING

The experiment is modeled with MAD-X and MICROMAP simulations. In both codes, the tracking is

performed using symplectic integration. In order to include the space charge forces, particles are subject to localized electric kicks. Detailed information about the applied frozen space charge models in MAD-X and MICROMAP can be found in [29] and Appendix A of [1], respectively.

In order to compare the results with the experimental findings, the output data of the simulations are treated with the same procedure as adopted for the experimental data.

Simulations and experimental results are presented in Fig. 5(a) for MAD-X, and in Fig. 5(b) for MICROMAP. We find a relatively good prediction of the maximum emittance growth for both codes.

Both codes provide the main features of the emittance growth. We observe that the prediction of beam loss is smaller than the experimental finding: beam loss in the experiment is 35%, but MICROMAP predicts 25%. A similar uncertainty has been found in all previous simulations when compared with experiments [1,2]. This emphasizes the difficulty of beam loss prediction in a realistic accelerator when a high intensity bunched beam is stored. In fact, beam loss depends on the accurate machine model, the fine details of beam size growth and the exact geometry of the machine. All these ingredients are difficult to determine, which complicates the simulations.

Furthermore, at the horizontal tune closest to the integer, MAD-X tracking reveals some emittance growth in the horizontal plane which is not present in the MICROMAP simulations.

In Fig. 6 the prediction of the two codes against the measured beam profiles at $Q_{x0} = 6.104$ is compared. Both codes agree on the final profiles.

This means that the physics of frozen space charge, although obtained with different algorithms, is computationally correctly modelled for describing the dynamics in the full PS accelerator structure. The comparison with respect to the experimental profiles shows that the prediction of the codes yields a less dense halo with respect to that found in the experiment. This difference most likely accounts for the limits of the modeling, which neglects the

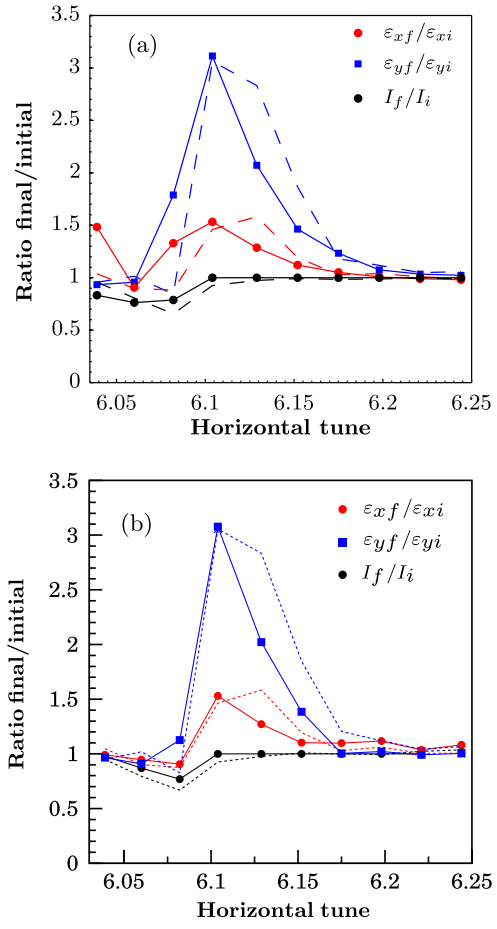

FIG. 5. (a) Emittance growth and beam survival as computed with MAD-X (adaptive mode). (b) Simulation results with MICROMAP (frozen mode). The quantities retrieved from the experimental data are shown with dashed lines in both cases.

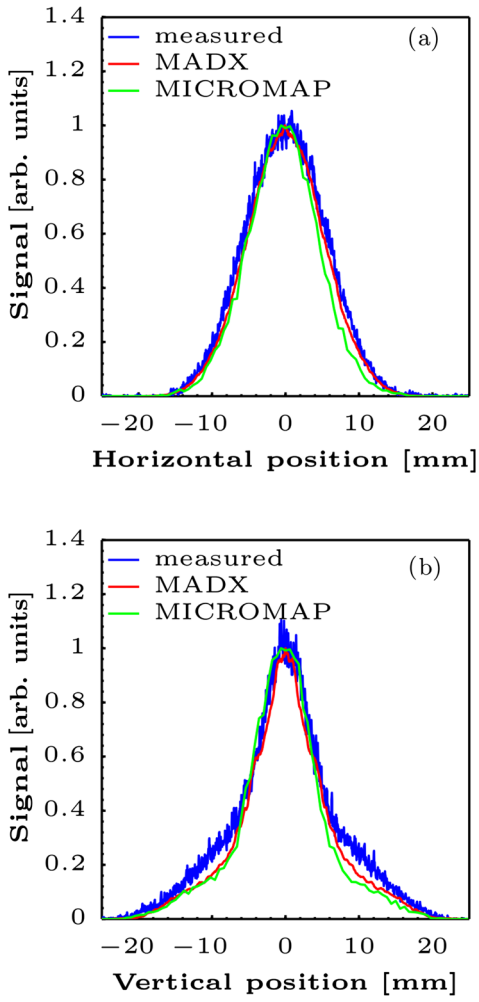

FIG. 6. Comparison between experimental and simulated final profiles for $Q_{x0} = 6.104$ in the (a) horizontal and (b) vertical plane.

self-consistent physics as it relies on the frozen space charge model.

V. SPACE CHARGE DETUNING AND RESONANCE

In the first subsection we address, in absence of chromatic effects, how the presence of space charge changes the effective distance from the resonance, hence its effect on the halo size.

In a second subsection we include the effect of natural chromaticity in the simulations (see Table II), as chromaticity is kept uncorrected during operation at low energy in the PS. It will be shown that nonzero chromaticity importantly impacts the particle dynamics in space charge dominated machines.

A. In absence of chromaticity

For any particle experiencing the tunes Q_x, Q_y as pointed out in Sec. III the resonance condition means $Q_x + 2Q_y - 19 = 0$. For arbitrary particle tunes Q_x, Q_y the resonance condition is in general not fulfilled, and we then consider as distance from the resonance the quantity $\Delta_r = Q_x + 2Q_y - 19$, which is a generalization of Eq. (1). In the present case under study the tunes of a particle also depend on its oscillation amplitude X, Y via the amplitude dependent tune-shift $\Delta Q_{\mathrm{sc,x}}(X,Y)$, $\Delta Q_{\mathrm{sc,y}}(X,Y)$. We approximate the distance from the resonance Δ_r for a particle as

$$\Delta_r = \Delta_{r0} + \Delta Q_{\mathrm{sc,x}}(X,Y) + 2\Delta Q_{\mathrm{sc,y}}(X,Y), \qquad (3)$$

and the resonance condition becomes $\Delta_r = 0$. Equation (3) shows that the quantity $\Delta Q_{\mathrm{sc,x}}(X,Y) + 2\Delta Q_{\mathrm{sc,y}}(X,Y)$ acts as an effective amplitude dependent detuning, which has to be included in the resonance condition, and incorporates the simultaneous effect of space charge on both planes. For a particle with $X=Y=0$ we have $\Delta Q_{\mathrm{sc,x}}(0,0)+2\Delta Q_{\mathrm{sc,y}}(0,0)=\mathcal{D}_{\mathrm{r,sc}}$. Given the distance from the resonance Δ_{r0} defined by the machine tunes Q_{x0}, Q_{y0}, the resonance condition $\Delta_r = 0$ identifies a set of resonant amplitudes (X,Y) in the weak third order resonance approximation.

Throughout this article we focus the discussion on the working point $Q_{x0} = 6.104$, $Q_{y0} = 6.476$, for which $\Delta_{r0} = 0.056$ and the largest emittance growth is observed in Fig. 3. In Fig. 7 we plot the space charge resonance detuning for particles located at $z = z' = 0$ in the longitudinal plane. Particle amplitudes are rescaled to the rms beam sizes at the location of the vertical wire scanner (SS64).

It is most relevant to determine the widest tune spread with respect to the horizontal and vertical planes. To this end we verify the two directions of amplitudes in the space (X,Y): along $\{(0,Y): 0 < Y/\sigma_y < 7.5\}$ for the black curve, and along $\{(X,0): 0 < X/\sigma_x < 7.5\}$ for the red curve. As expected we find that $\Delta Q_{\mathrm{sc,x}} + 2\Delta Q_{\mathrm{sc,y}}$ is approximately the same in both curves for amplitudes in the core of the beam, but starts to deviate at larger amplitudes. This is the typical behavior to be expected from detuning with amplitude due to space charge and stems from the different average beam size ratio $r_x/r_y = 1.87$, and because of the specific resonance under study. From Fig. 7 we find the resonant amplitudes to be at $X = 0, Y \simeq 3.9\sigma_y$, and at $X \simeq 4.6\sigma_x$, $Y = 0$ (indicated by the intercepts with the line at $\Delta_r = 0$).

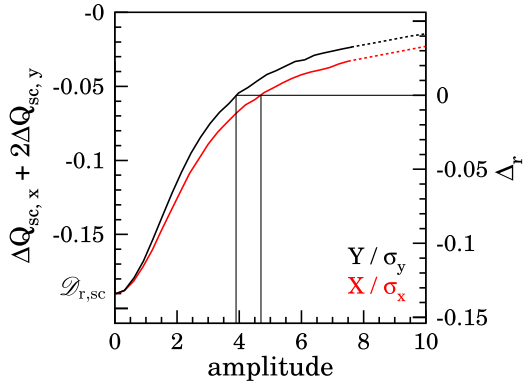

FIG. 7. Resonance detuning $\Delta Q_{\mathrm{sc,x}} + 2\Delta Q_{\mathrm{sc,y}}$ and Δ_r as a function of amplitudes $(0,Y)$ (black curve), and $(X,0)$ (red curve). The amplitudes are computed at the location of the vertical wire scanner (SS64).

These resonant amplitudes are computed for the longitudinal position $z = 0$, where the space charge is strongest. At any other longitudinal section of the bunch the space charge is weaker, and resonant amplitudes will be smaller. This suggests that the maximum extension of the halo is equal to the largest of these resonant positions as determined from Fig. 7. The argument is similar to the one presented in [2].

This interpretation can be directly verified by comparing the beam profiles obtained from simulations in which the chromaticity was set to zero. In Figs. 8(a) and (b) we plot the horizontal and vertical beam profiles, respectively, at the location of the wire scanner in SS64 normalized with the transverse rms beam sizes. The blue curves are the initial profiles, and the black curves are the final profiles after 1.1 s of storage time. We find that the edge of the halo formed in the vertical plane is at $\simeq 3.5\sigma_y$, a value consistent with the analysis of the amplitude dependent detuning, which yields $\simeq 3.9\sigma_y$. The small difference in amplitude can be attributed to the resonance strength, which changes the locations satisfying the resonant condition. The horizontal beam profile, however, does not exhibit any trace of halo, contrarily to the expected halo reaching $X \simeq 4.6\sigma_x$ according to Fig. 7. This shows that a more complex mechanism is at work than the one we have described up to now.

B. Effect of the chromaticity

In the previous section the effect of the chromaticity was neglected, and the maximum halo size in the vertical

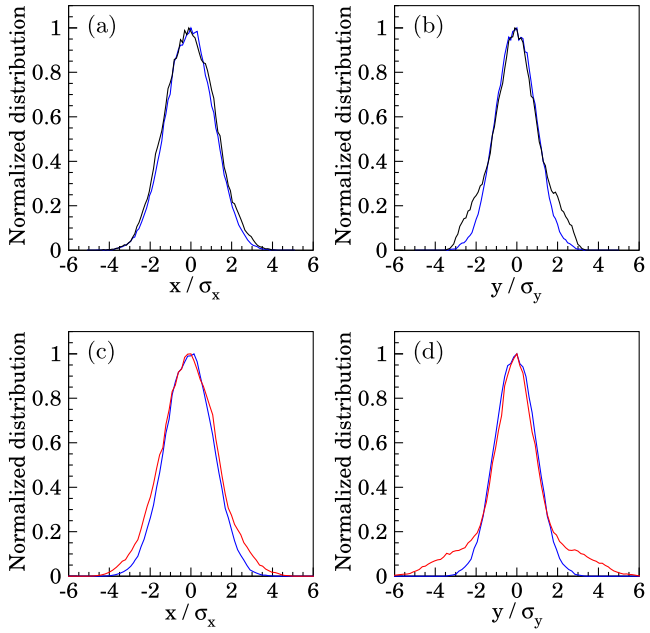

FIG. 8. Pictures (a) and (b) show the horizontal and vertical beam profiles in simulations with the chromaticity set to zero. The working point is $Q_{x0} = 6.104$, $Q_{y0} = 6.476$. The blue curves are the initial profiles while the black curves are the final profiles. Pictures (c) and (d) represent the same settings, but including the chromatic effect. These beam distributions are computed at the location of the vertical wire scanner. In this case the final profiles are shown in red.

plane was found to be $3.5\sigma_y$ (see Fig. 8(b)). However, in Figs. 8(c) and (d) the results of the same simulations including natural chromaticity show a different halo size extending to $Y \simeq 5.5\sigma_y$, again present mostly in the y plane. The full comparison of the beam response to the presence of natural chromaticity is shown in Fig. 9.

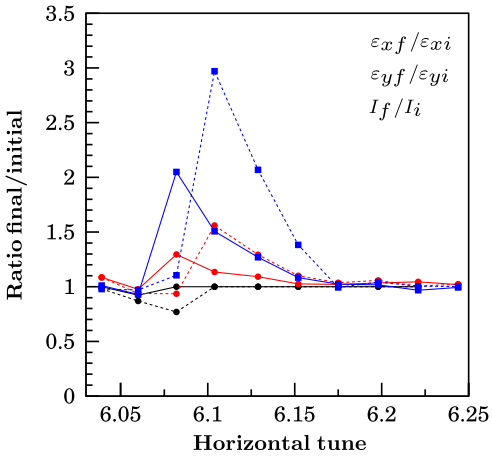

FIG. 9. Simulated growth of horizontal and vertical emittance with the chromaticity set to zero (solid lines), and including natural chromaticity (dashed lines). The simulations are done with MICROMAP.

The dashed curves show simulations including natural chromaticity, while the solid curves correspond to the results of simulation with zero chromaticity. The presence of chromaticity creates a dramatic enhancement of the emittance growth combined with a shift of the Q_{x0} at which the maximum emittance blow-up occurs.

We attempt to evaluate the change in the halo size, hence of emittance, by using the resonance detuning including space charge and the effect of the natural chromaticity. The chromaticity on one particle with off-momentum $\delta p/p$ yields a tune-shift of $\delta Q_{x,y} = Q'_{x,y}\delta p/p$ and the contribution of this tune-shift to the distance from the resonance Δ_r is $\delta Q_x + 2\delta Q_y = (Q'_x + 2Q'_y)\delta p/p$. Therefore, we obtain $|\delta Q_x + 2\delta Q_y| \leq 0.038$ considering the natural chromaticity for any particle in a longitudinal parabolic distribution. This means that a particle with the maximum chromatic tune shift will experience a shift in resonance detuning of 0.038. This is equivalent to shifting the Δ_r axis as shown in Fig. 10, and the halo size becomes $Y \sim 9\sigma_y$ as indicated by the interception of the "continuation" of the black curve to $\Delta_r = 0$. For the sake of the argument the curves had to be smoothly extended beyond the regime that is accessible via the simulations.

This does not agree with the result shown in Figs. 8(c) and (d) in which the final beam profiles (red curves) are obtained from simulations including the effect of natural chromaticity, yielding a maximum halo located at $\simeq 5.5\sigma_y$. We have to conclude that the analysis is still not sufficient to fully explain the experimental results with simulations and in particular the asymmetry of the halos between the transverse planes. In the following section we will present an in-depth inspection of the 2D dynamics of the coupled sextupole resonance that will allow us to overcome the remaining discrepancies.

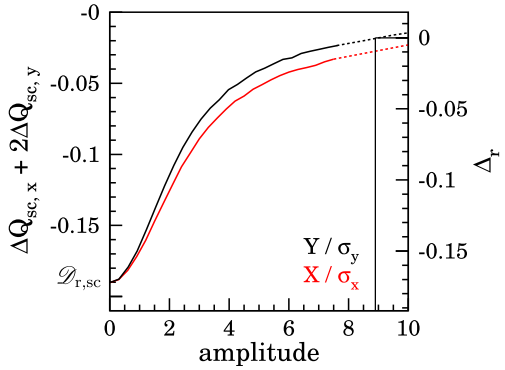

FIG. 10. Resonance detuning $\Delta Q_{\mathrm{sc,x}} + 2\Delta Q_{\mathrm{sc,y}}$, and Δ_r as a function of amplitudes $(0, Y)$ (black curve), and $(X, 0)$ (red curve) including chromaticity. The working point is $Q_{x0} = 6.104$; the vertical line corresponds to the halo edge of $Y \sim 9\sigma_y$. The amplitudes are computed at the location of the vertical wire scanner (SS64).

VI. ROLE OF THE FIXED-LINES

For 1D resonances the phenomena of trapping/scattering is caused by the migration of instantaneous islands due to synchrotron motion and space charge [1,2,30].

In the case of a 2D resonance the full discussion on trapping/scattering is more complex and goes beyond the purpose of this paper. Nevertheless, we discuss here the origin of the asymmetric halo with respect to the transverse planes, and address the discrepancies found in the previous section.

A. The fixed-lines in absence of space charge

In the proximity of the resonance $Q_x + 2Q_y = 19$ the 2D nonlinear dynamics differs from the case of one dimensional resonances. At any location s, the resonant particles are locked on a curved closed line extending over the 4 dimensions of the transverse phase space. Turn after turn, resonant particles move along this orbit, which is referred to as fixed-line.

The theory of the fixed-lines is discussed in Refs. [13,15,16,19–22,31], and in Ref. [14] the main properties of these objects have been derived. According to the theory a fixed-line is parametrized as

$$x = \sqrt{\beta_x a_x}\cos(-2t - \alpha + \pi M),$$
$$y = \sqrt{\beta_y a_y}\cos(t). \tag{4}$$

The coordinates x', y' are readily derived from Eq. (4). The fixed-line emittances a_x, a_y are determined by the distance to the resonance Δ_{r0}. The variable t parametrizes the fixed-line. In absence of space charge and of nonlinear detuning, stable fixed-lines have the largest extension in the y direction, and in particular the ratio of the fixed-line invariants takes the value of $a_y/a_x = 8$ when a_y is maximum (see Ref. [14]). Rescaling this aspect ratio with the rms beam sizes at the section of the vertical wire scanner in SS64 yields $[Y/\sigma_y]/[X/\sigma_x] \simeq 3.6$, which is our reference for comparing the effect of space charge on fixed-lines. The coefficient α in Eq. (4) controls the orientation of the fixed-line. It depends on the location of the nonlinear errors and therefore on the phase of the driving term with respect to the 2D Poincaré surface of section. The integer M is related to the condition of existence of the fixed-line (see Ref. [14]). In absence of space charge a relevant result from the theory of the fixed-lines states that there are infinite fixed-lines in the proximity of the resonance $Q_x + 2Q_y = 19$. Certainly the presence of space charge alters the theory via additional nonresonant terms in the slowly varying Hamiltonian. But the existence of more than one fixed-line remains unchanged as we will show with the following numerical study.

B. Resonance stop-band in absence of space charge

We first determine the resonance stop-band. For several machine tunes starting from $Q_{x0} = 6.104$, $Q_{y0} = 6.476$ and along the direction of the space charge tune-spread we estimate the volume of the 4D nonlinear phase space acceptance in absence of space charge. We proceed by filling the PS linear acceptance with uniformly distributed particles and track this beam for 10'000 turns. The number of surviving particles is proportional to the stable volume in phase space. Figure 11 shows the ratio N/N_0 (i.e. the fractional volume of stable initial conditions) as a function of Δ_{r0}. We note that the fraction of beam survival is larger than $N/N_0 = 0.35$: the fact that the stable phase space volume does not approach zero for $\Delta_{r0} \to 0$ stems from the detuning created by the nonlinear elements which are not resonant. These elements, for example octupolar components present in the PS lattice, cause a detuning, which creates a small shift of the resonance also visible in Fig. 11. From this figure we can quantify the effective resonance stop-band to be $\mathcal{D}_{\mathrm{r,sb}} \sim 0.02$ in terms of Δ_{r0}. Comparison with $|\mathcal{D}_{\mathrm{r,sc}}| = 0.19$ shows that the resonance is weakly excited. (see Appendix C for a discussion on $\mathcal{D}_{\mathrm{r,sc}}$).

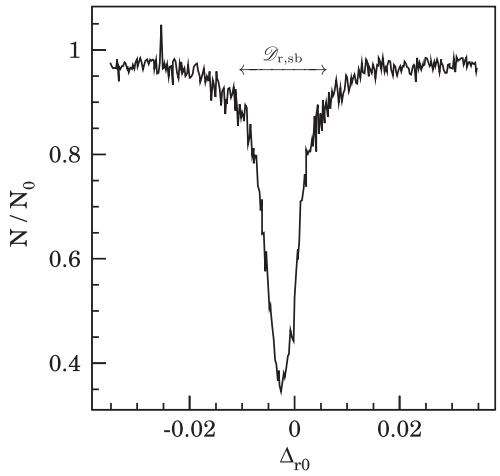

FIG. 11. Resonance stop-band.

C. Frozen tori and space charge

1. In the absence of chromaticity

In Fig. 12 we plot the overlap of a simulated space charge tune-spread with the resonance line $Q_x + 2Q_y = 19$, which is excited by a current of $I = 2$ A, for the working point $Q_{x0} = 6.104$, $Q_{y0} = 6.476$. In this simulation the chromaticity is set to zero and the tunes are computed for test particles placed on a radial $x - y$ grid with initial coordinates

$$x_{ij} = \frac{6i}{30}\sigma_x \cos\left(\frac{2\pi j}{40}\right)$$
$$y_{ij} = \frac{6i}{30}\sigma_y \sin\left(\frac{2\pi j}{40}\right), \tag{5}$$

where the indices extend between $0 \le i \le 30$ and $0 \le j \le 40$. The remaining coordinates for all test particles are $x'_{ij} = y'_{ij} = z_{ij} = z'_{ij} = 0$. The effect of the resonance on

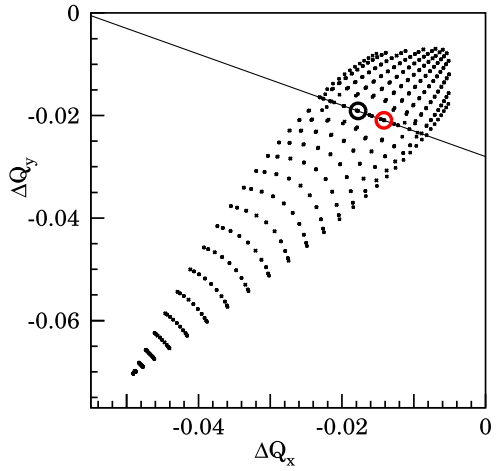

FIG. 12. Space charge tune-spread. The solid line is the third order coupled resonance $Q_x + 2Q_y = 19$. The circles enclose the tunes of the two resonant orbits shown in Fig. 13(a).

the single particle tunes clusters them on the resonance line.

An inspection of the resonant orbits in Fig. 12 reveals that particles initially located near $x = 0$ exhibit the strongest resonance signature. For our discussion we select the two resonant orbits of largest vertical size and their tunes are indicated by the two circles. Figure 13(a) shows the $x - y$ projection of these two resonant orbits (their color corresponds to the one of the two circles in Fig. 12). The resonant feature becomes apparent by the figure-of-eight shapes in the $x - y$ projections, which are consistent with Eq. (4) for $\alpha \sim \pi/2$ and $M = 0$. This suggests that the orbits in Fig. 13(a) are tori enclosing two distinct fixed-lines.

The resonant orbits shown in Fig. 13(a) exhibit the aspect ratio of $[Y/\sigma_y]/[X/\sigma_x] \simeq 110$ for the red dots, and of $[Y/\sigma_y]/[X/\sigma_x] \simeq 60$ for the black dots. Both aspect ratios are different from the expected ratio of 3.6 previously discussed for the case of a single 3rd order resonance. Unavoidably, this is the result of the presence of space charge and other machine nonlinearities.

Figure 13(a) further highlights a very important feature: the orbit with maximum amplitude (black) has a vertical amplitude of $3.5\sigma_y$, which is exactly the edge of the halo found in Fig. 8(b). However, no final conclusion can be drawn as the red resonant orbit depicts a different maximum y amplitude. We will come back to this issue later in this section.

Due to the synchrotron motion, the position of the "instantaneous" fixed-line changes. This can be seen in Fig. 13(b), which is obtained for the same bunch, but with the grid of test particles now located at $z = 1.5\sigma_z$, hence with less transverse space charge (for this simulation the longitudinal motion is kept frozen). The two vertically largest resonant orbits are now smaller. The different aspect ratio with respect to the orbits in Fig. 13(a) may be due to the fact that we used the same grid, but now the space

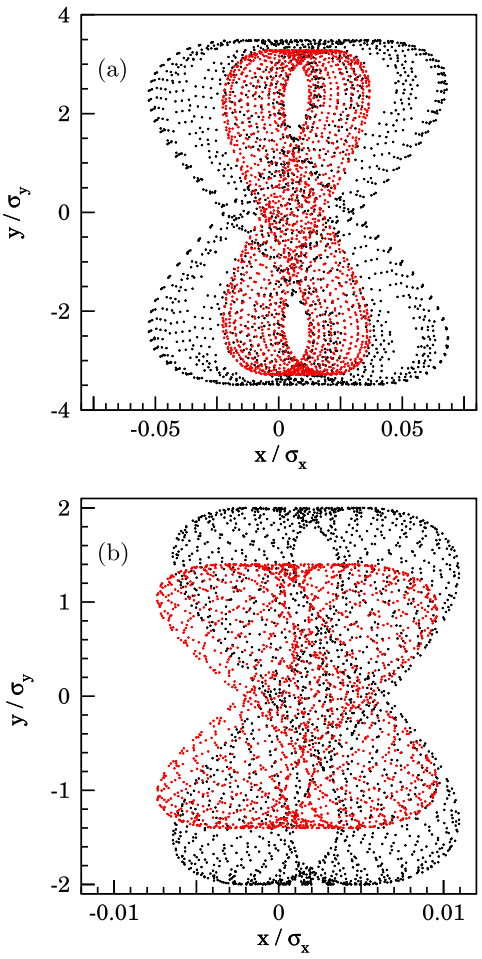

FIG. 13. (a) Resonant orbits of two particles (black & red) at the longitudinal position $z = z' = 0$. (b) Resonant orbits for two particles (black & red) at longitudinal position $z = 1.5\sigma_z$ and $z' = 0$. The synchrotron motion is kept frozen.

charge is approximately 3 times smaller, whereas the machine working point and resonance strength remains unchanged. Consequently we do not select the "same" fixed-lines as those at $z = 0$.

Figures 13(a) and (b) demonstrate that the synchrotron motion moves particles through transverse sections where the instantaneous fixed-lines have different spatial extension (because their size stems from a combination of the transverse space charge tune-spread and of machine tunes). In particular, fixed-lines at $z = 0$ are larger than those fixed-lines at $z = 1.5\sigma_z$.

2. Effect of the chromaticity

In order to investigate the effect of chromaticity on the resonant orbits, we have repeated the previous simulations applying the same procedure. The coordinates of the test particles were initialized according to Eq. (5), with $x'_{ij} = y'_{ij} = z_{ij} = 0$. However, the momentum of the particles was artificially shifted by $\delta p/p = 2\sigma_{\delta p/p}$, and the synchrotron motion was kept frozen.

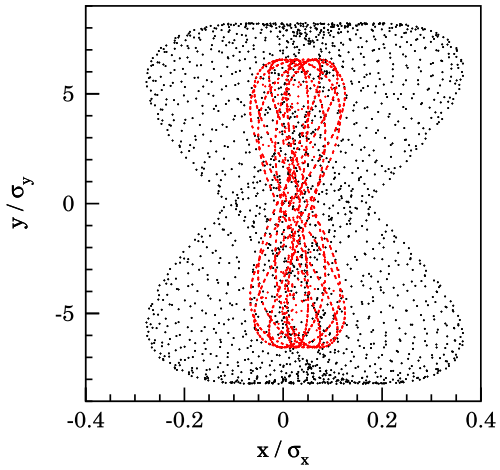

FIG. 14. Resonant orbits for particles having longitudinal momentum $\delta p/p = 2\sigma_{\delta p/p}$, and $z = 0$. In the simulation the longitudinal motion is kept frozen.

Among all particles, those two following the resonant orbits with the largest vertical size are shown in Fig. 14. They exhibit different aspect ratios compared to the results shown in Fig. 13(a), as they move around two different fixed-lines. It has to be noted that the maximum vertical amplitude of the red orbit agrees with the extent of the halo size found in the profile of Fig. 8(d). This result shows that the chromaticity plays a fundamental role in increasing the size of resonant orbits.

D. Periodic crossing of fixed-lines

The above discussed numerical simulation results show *particle trajectories that periodically cross fixed-lines*. As in the case of 1D resonances this mechanism is created by the coexistence of space charge detuning and synchrotron motion.

In each transverse section located at position z in the bunch frame, the "resonance detuning" $\mathcal{D}_{\mathrm{r,sc}}(z)$ is obtained by scaling the maximum resonance detuning $\mathcal{D}_{\mathrm{r,sc}} = -0.19$ with the respective local line-charge density $\rho(z)$, according to

$$\mathcal{D}_{\mathrm{r,sc}}(z) = \mathcal{D}_{\mathrm{r,sc}} \frac{\rho(z)}{\rho(0)}. \tag{6}$$

The quantity $\mathcal{D}_{\mathrm{r,sc}}(z)$ allows to discuss the periodic crossing of fixed-lines. Considering, for example, a Gaussian longitudinal profile and a particle located at $z = 2\sigma_z$, the space charge tune-spread is $\mathcal{D}_{\mathrm{r,sc}}(2\sigma_z) = -0.0257$. At the beginning of motion this particle is therefore not resonant as $\Delta_r = \Delta_{r0} + \mathcal{D}_{\mathrm{r,sc}}(2\sigma_z) = 0.0303 > 0$ [see also Eq. (3)]. As the particle moves toward the longitudinal centre of the bunch, the space charge increases and the particle will encounter a threshold longitudinal position z^* satisfying $\Delta_{r0} + \mathcal{D}_{\mathrm{r,sc}}(z^*) = 0$. At that longitudinal position, the third order resonance acts on the transverse plane, and fixed-lines emerge from the transverse beam center. Continuing the motion, the amplitudes of the fixed-lines will increase reaching the maximum at $z/\sigma_z = 0$ (where space charge is maximum). At the longitudinal position $z = -z^*$, the fixed-lines will again collapse to the transverse origin as the relation $\Delta_{r0} + \mathcal{D}_{\mathrm{r,sc}}(-z^*) = 0$ is again satisfied. Therefore, fixed-lines emerge or collapse from the transverse plane four times per synchrotron oscillation.

Depending on the speed of resonance crossing (adiabatic or non-adiabatic), particles can be trapped or scattered by the fixed-lines. For a fixed-line crossing the particle orbit adiabatically, the particle is trapped by the resonance and follows the fixed-line. In the case of nonadiabatic crossing, the particle invariant experiences a kick due to the resonance. This process is referred to as scattering.

1. Scattering processes

In order to discuss scattering phenomena, we select one test particle from the simulations presented in Fig. 8(a) and 8(b), with initial coordinates such that $\varepsilon_x/\varepsilon_{x,\mathrm{rms}} = 2.8$, $\varepsilon_y/\varepsilon_{y,\mathrm{rms}} = 2$, and $z/\sigma_z = -2$, $z' = 0$. Figures 15(a) and 16(a) show the time evolution of the normalized single particle Courant-Snyder invariants. A diffusional process is clearly visible, which is caused by the scattering due to the periodic resonance crossing. We observe that these two curves are correlated. From this we conclude that the same diffusion process is active in both planes.

Figures 15(b) and 16(b) show a detailed view of the invariant during one synchrotron oscillation: the resonance crossing due to space charge and synchrotron motion appears as a jump of the Courant-Snyder invariant four times per synchrotron oscillation. For the parameters used in simulations we obtain $z^*/\sigma_z = 1.563$, and the four points at which fixed-lines emerge or collapse are indicated by the blue vertical lines. The correlation of the jumps is due to the simultaneous action of the fixed-line in both $x - x'$ and $y - y'$ planes.

The asymmetric form of the $x - y$ projection of the resonant orbits readily explains the asymmetry of the beam profiles shown in the simulations of Fig. 8(a) and (b). Very likely this is also the explanation of the asymmetry of the measured halo shown Fig. 4(b) and (d).

2. Trapping processes

Considering the above discussed simulations, the adiabatic trapping process does not occur naturally. In order to study this regime, additional simulations with an artificially long synchrotron oscillation period of 10^7 turns were performed. We consider one test particle at $z = -2\sigma_z$ inside the bunch, with the other initial conditions being $y \simeq 0.5\sigma_y$ and $x = x' = y' = z' = 0$.

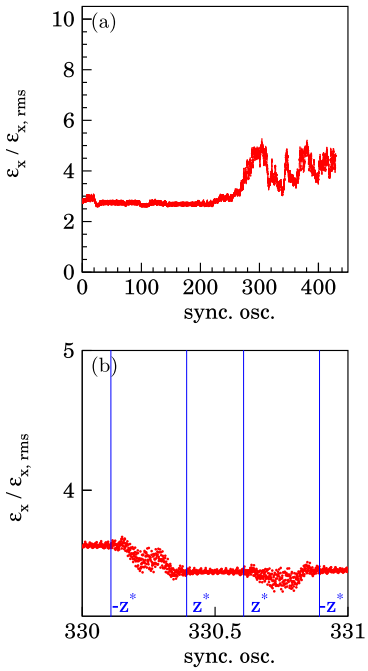

FIG. 15. (a) Evolution of the horizontal Courant-Snyder invariant of a test particle over 430 synchrotron oscillations. (b) Evolution of the horizontal invariant over a single synchrotron period, experiencing four resonance-induced kicks.

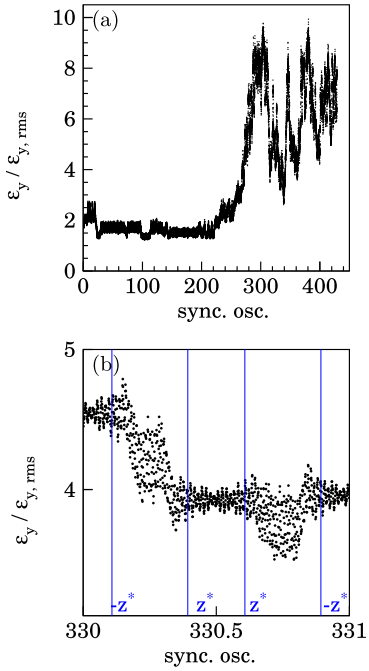

FIG. 16. (a) Evolution of the vertical Courant-Snyder invariant of a test particle over 430 synchrotron oscillations. (b) Evolution of the vertical invariant over a single synchrotron period, experiencing four resonance-induced kicks.

This particle is tracked over one quarter of a synchrotron oscillation (including space charge) and the results of adiabatic resonance crossing are shown in Fig. 17.

In Fig. 17(a) 10 snapshots of the horizontal and vertical particle coordinates, each corresponding to 1000 consecutive turns, are shown. The time interval in between the different snapshots has been equally spaced. For five of these 10 sets, i.e., for those with $z > z^*$, the motion is apparently locked on fixed-line structures (the instantaneous fixed-line) with approximately the same horizontal to vertical aspect ratio. The closer the particle is to the bunch center, the larger the fixed-line becomes and its maximum size is reached at $z = 0$. The red lines are obtained from Eq. (4) by computing a_x, a_y from the machine optics and particle coordinates. The value of α for all curves is 1.6645 rad.

In Fig. 17(b) the simulation is repeated, but including the natural chromaticity. The simulation is prepared so that the particle reaches the off-momentum of $\delta p/p = 2\sigma_{\delta p/p}$, the maximum off-momentum in the bunch, at $z = 0$. We now obtain six fixed-line structures in the set of 10 snapshots. In order to obtain z^* in this case, the effect of the chromaticity has to be included in Eq. (3).

The aspect ratio of the fixed-lines in Fig. 17 is ~1.8, the maximum extension of the y direction is $\sim 3\sigma_y$ with zero chromaticity, and up to $\sim 6\sigma_y$ when including the natural chromaticity. These results differ significantly from the values shown in Figs. 13 and 14.

The largest fixed-line of Figs. 17(a) and (b) are consistent with the halo extension obtained with the multiparticle simulations shown in Figs. 8(b) and (d): the halo in the vertical plane and the core growth in the horizontal plane can therefore be explained by the geometry of the largest adiabatic fixed-line.

A systematic analysis of the motion of particles starting at $z = -2\sigma_z$ shows that, according to their initial conditions, particles are trapped by different and distinct fixed-lines. However, as particles approach $z = 0$ they all *"verge"* close to the same largest fixed-line. Therefore this fixed-line, the largest in Figs. 17(a) and 17(b), defines an *adiabatic limit*.

E. Discussion

In the case of a 1D third order resonance, the maximum extension of the halo is given by the outer separatrices of the three instantaneous islands at $z = 0$, where the space charge is maximum. The results presented in this article suggest a more complex scenario in the case of 2D resonances.

The arguments of Sec. VI C suggest that the preferential plane of larger halo extension is related to the form of the fixed-line. However, in the same section we find evidence that several instantaneous fixed-lines exist, but their sizes are not consistent with the beam halo from simulations, even including chromaticity. In fact, the largest instantaneous fixed-line of Fig. 14, obtained by freezing the synchrotron motion, reaches an

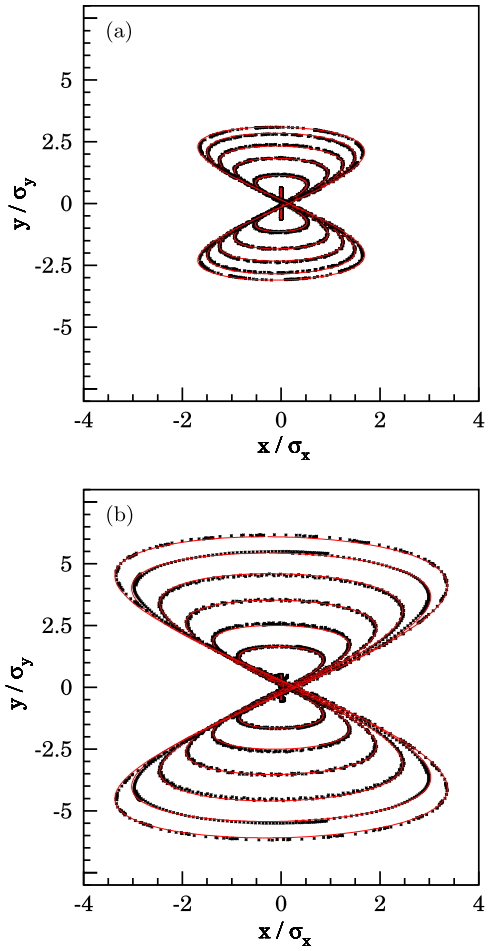

FIG. 17. (a) Sequence of fixed-lines constructed by a particle moving from $z = -2\sigma_z$ to $z = 0$. (b) Same as in (a) but with the natural chromaticity included in the simulation. In both cases the red curves are obtained from Eq. (4) with one value of α.

amplitude $8\sigma_y$. This is not consistent with the halo extension found in the simulation presented in Fig. 8(d), where the halo extends up to $5.5\sigma_y$. This is mainly because those fixed lines where found by freezing the synchrotron motion, without considering the full dynamics. This suggest that not all fixed-lines participate equally to the dynamics.

An indication of the fixed-lines participating to the dynamics is obtained in Sec. VI D 2 via an artificial adiabatic resonance crossing process. We find that trapped particles stay on distinct fixed-lines, which converge all to the same largest fixed-line independently of their initial condition. For these processes, particles always reach a vertical halo size of $\simeq 6\sigma_y$, which is consistent with Fig. 8(d).

The details of the various simulation results suggest the following: (1) The instantaneous fixed-lines found from the adiabatic crossing identify the main fixed-lines, which could be responsible for creating the stochastic process leading to an asymmetric halo during the nonadiabatic periodic crossing. (2) In the adiabatic limit, the instantaneous fixed-lines define the edge of halo particles for the scattering process. This is visible in Figs. 15 and 16 at the end of the simulations, where the spatial aspect ratio of $\simeq 1.8$ is consistent with the adiabatic crossing.

VII. CONCLUSION AND OPEN QUESTIONS

In this article, experimental and simulation studies of the beam dynamics of space charge dominated beams close to the coupled third order resonance $Q_x + 2Q_y = 19$ are reported. The results of measurements, which were carried out in the CERN PS, have shown a remarkable asymmetric beam halo formation.

In order to understand these findings a code benchmarking between MAD-X and MICROMAP was carried out. Applying a purely frozen space charge mode, good agreement between the predictions obtained by the two codes was found.

The agreement between the experimental data and the simulations at the various working points is very good. In particular, the beam profiles for the most relevant working point, i.e., the one exhibiting the largest emittance increase, were benchmarked.

The presented study leads to the conclusion that halo formation occurs due to periodic resonance crossings, which has already been established for 1D resonances. However, a 2D resonance creates a web of fixed-lines, and the periodic motion of particles inside the bunch generates a periodic crossing of some of these fixed-lines. Our study shows a direct link between fixed-lines and halo formation. In particular, the $x - y$ projection of the fixed-lines reveals an aspect ratio consistent with the measured and simulated asymmetry of the halo.

The phenomenological observation of the existence of an adiabatic limit, which defines the halo edge in the scattering regime, remains to be investigated more thoroughly.

On an applied level, our study gives us confidence that the beam halo formation is predictable for space charge dominated beams close to coupled resonances as long as the machine modeling is accurate enough. The discussions on the dynamics as addressed here will become an essential tool to interpret simulations, and develop mitigation strategies when full resonance compensation is not possible.

ACKNOWLEDGMENTS

The authors would like to acknowledge the help of the PS operations crew for the preparation of the beam used in the experiment. We are furthermore grateful to G. Arduini, I. Papaphilippou, and G. Sterbini for fruitful discussions. The research leading to these results has received funding from the European Commission under the FP7 Research Infrastructures project EuCARD-2, Grant Agreement No. 312453.

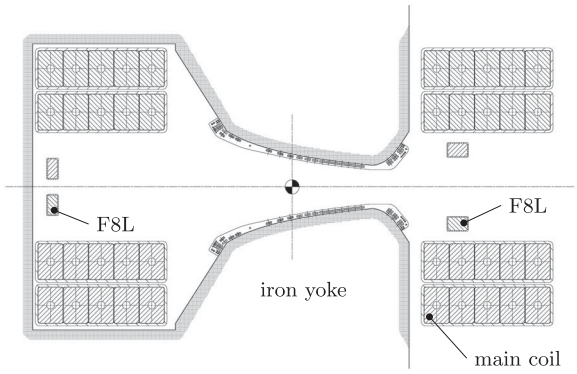

FIG. 18. Cross section of one MU of the PS. The reference point between the two poles corresponds to the location of the closed orbit. The circuits of the PFW, which are encapsulated by an epoxy resin, are situated directly on top of the poles. Furthermore, the main coils and the F8L are visible [33].

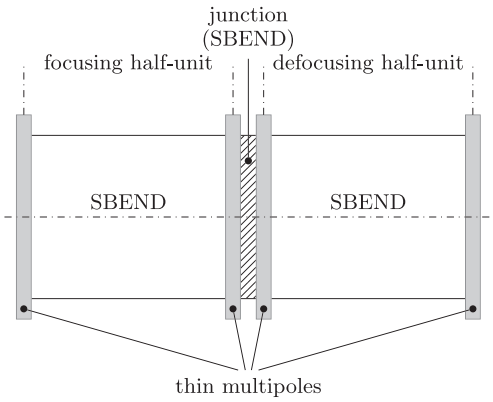

FIG. 19. Modeling of the PS MU. Even though the junction between the two half-units is included as SBEND, it is actually just a drift space.

APPENDIX A: THE CERN PROTON SYNCHROTRON

The PS [32] has a circumference of $2\pi \times 100$ m and is composed of 100 combined function magnet units (MUs), which are interleaved by 100 straight sections (SSs). Each MU consists of a focusing and a defocusing half-unit and their overall arrangement results in a FOFDOD lattice. Additional elements, such as devices for injection and extraction, accelerating cavities and auxiliary magnets, are located in the different SSs.

In order to control betatron tunes and linear chromaticities additional circuits are placed on top of the magnetic poles of each MU. These pole face windings (PFW) are divided into narrow and wide windings for each half-unit and the naming convention refers to the width of the air gap at the position of the respective circuit (see Fig. 18).

Furthermore, each MU contains the figure-of-eight loop (F8L), which is an additional circuit that crosses between the two half units giving the corresponding shape. In contrast to these smoothly distributed elements 40 low energy quadrupoles (LEQ) are installed to control both transverse tunes from injection kinetic energy at 1.4 GeV up to a kinetic energy of about 3.5 GeV. The individual circuits of the PFW, the F8L and the LEQ are powered independently, offering high flexibility during machine operation.

1. Modeling of the PS lattice

In order to model this complex lattice in the most realistic way in simulations, each MU is made up of two sector bending magnets (SBENDs) as shown in Fig. 19. In addition to the dipole component, each SBEND is assigned with either a focusing or a defocusing quadrupolar component to model the combined function magnet. Moreover, two thin multipoles are inserted in every half-unit [34]. Based on measurements of the machine tunes, linear and nonlinear chromaticities, these multipolar components are then used to build an effective nonlinear model of the accelerator. Below a kinetic energy of 3.5 GeV, i.e., in the regime where the PFW are not used during operation, the PS behaves rather linearly and the multipoles are mainly used to match linear chromaticity. For the simulations presented in this article the dependency of the transverse tunes on the relative momentum error was modeled as:

$$Q_x\left(\frac{\delta p}{p}\right) = Q_x - Q'_x\frac{\delta p}{p} + \frac{1}{2}Q''_x\left(\frac{\delta p}{p}\right)^2 \tag{A1}$$

$$= 6.25 - 5.30\frac{\delta p}{p} + \frac{1}{2}27\left(\frac{\delta p}{p}\right)^2 \tag{A2}$$

$$Q_y\left(\frac{\delta p}{p}\right) = Q_y - Q'_y\frac{\delta p}{p} + \frac{1}{2}Q''_y\left(\frac{\delta p}{p}\right)^2 \tag{A3}$$

$$= 6.28 - 7.02\frac{\delta p}{p} + \frac{1}{2}35\left(\frac{\delta p}{p}\right)^2, \tag{A4}$$

where Q''_i is the almost negligibly small second order chromaticity. At higher energy, the thin multipoles allow to reproduce the nonlinearities of higher order introduced by the PFW (see also [23]).

The two sextupoles in SS39, which were used to excite the resonance in a controlled way, are implemented as thin lenses in the proper locations.

Due to the unavailability of measured magnetic errors of the MUs, no random components are included in the simulations. However, magnetic measurements of spare magnets as well as 3D simulation studies of the MUs have been started, which will allow further improvement of the modeled lattice.

APPENDIX B: PREPARATION OF THE RAW DATA

In order to analyze the transverse profiles in a consistent manner, a general treatment was required for all raw data

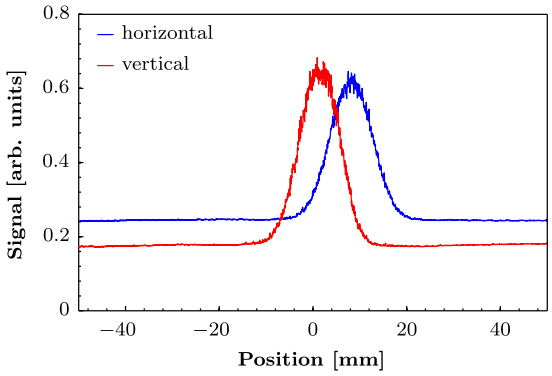

FIG. 20. Typical set of initial transverse profiles measured with the wire scanners. The offset of the baseline is clearly visible in both planes. The horizontal profile also exhibits a position offset due to the closed orbit distortion at the location of the wire scanner. Both offsets were removed prior to further treatment of the signals.

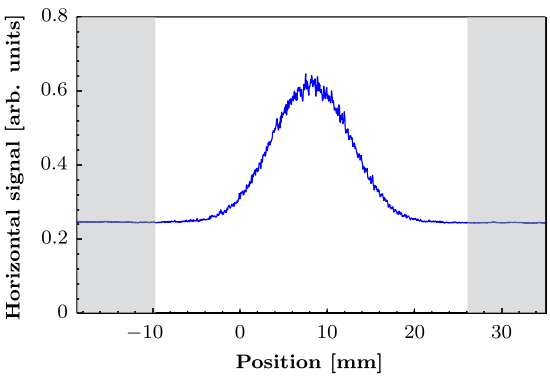

FIG. 21. This profile corresponds to the horizontal one of Fig. 20; however, only data points within the restricted interval $[-6\sigma_1+\mu_1, 6\sigma_1+\mu_1]$ are shown. The shaded areas indicate data points, which are considered for the evaluation of the baseline using $\mathcal{F}_2(z)$.

sets obtained from the wire scanner systems. Every profile consists of multiple bins, which are spaced by 50 μm and Fig. 20 shows an example of horizontal and vertical measurements at the beginning of the plateau at a kinetic energy of 2 GeV. For all studied working points the initial beam profiles were found to be Gaussian in both planes. One notices that the horizontal signals are not centred around zero due to the nonzero closed orbit. The significant offsets of the baselines are caused by the electronics of the wire scanners. To deal with the large "case-by-case" variation of the measured final beam profiles, it was necessary to devise a general treatment method.

The profile data returned by the wire scanner systems have a size of 100 mm in both transverse planes. Usually, the beam size is small compared to this value and, in order to extract only relevant information from the measurements, a useful data window had to be defined. Therefore, an estimate of the location of the peak and of the size of the beam profiles was obtained by using the following fitting function and applying a nonlinear least square method:

$$\mathcal{F}_1(z) = \alpha + \beta z + \frac{\gamma}{\sqrt{2\pi}\sigma_1} e^{-\frac{1}{2}\left(\frac{z-\mu_1}{\sigma_1}\right)^2}, \tag{B1}$$

where z corresponds to either the horizontal or the vertical plane. The fitting parameters α and β model the baseline, γ the amplitude, μ_1 the position of the peak, and σ_1 the standard deviation. Using the obtained mean value and standard deviation, only data points within the interval $[-6\sigma_1+\mu_1, 6\sigma_1+\mu_1]$ were considered for further analysis.

In order to improve the identification of the baseline, only data points within the interval $[-6\sigma_1+\mu_1, -4\sigma_1+\mu_1] \cup [4\sigma_1+\mu_1, 6\sigma_1+\mu_1]$ (see Fig. 21) were taken into account and an additional linear fit function

$$\mathcal{F}_2(z) = \delta + \kappa z, \tag{B2}$$

was applied. Thereby, the parameters α and β were reevaluated using a reduced data set. This approach was chosen to minimize the impact of baseline noise at large amplitude.

Subsequently, $\mathcal{F}_2(z)$ was subtracted from the data set and another fit using the Gaussian function

$$\mathcal{F}_3(x) = \frac{\lambda}{\sqrt{2\pi}\sigma_2} e^{-\frac{1}{2}\left(\frac{x-\mu_2}{\sigma_2}\right)^2}, \tag{B3}$$

was performed in order to determine the location of the peak of the profile with increased precision and to center the data by removing the contribution of the nonzero closed orbit. For the case of clean Gaussian raw data this procedure is shown in Fig. 22.

Lastly, only data points exceeding a threshold amplitude of $N_{\text{thr}} = 3\%$ of the maximum signal were considered (see Fig. 23) to remove negative data resulting from baseline noise. The choice of 3% as an appropriate value was based

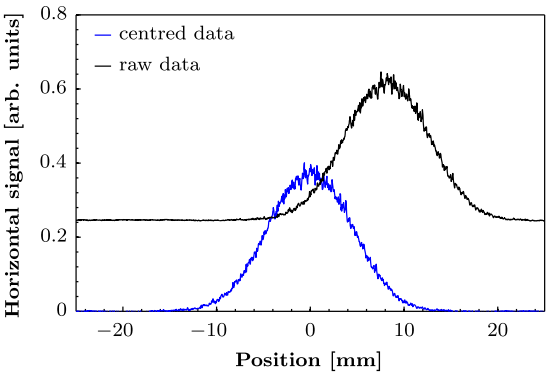

FIG. 22. After removing the contribution of the baseline and the horizontal offset, the profile depicted in blue is obtained. For comparison the horizontal raw data is shown as well.

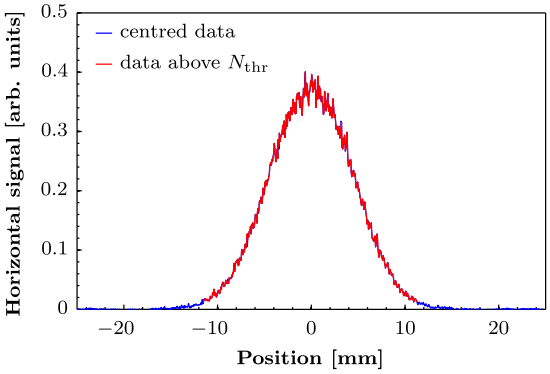

FIG. 23. In order to compute the statistical moments only data points above the defined threshold were considered.

on the maximum baseline noise that was observed for the whole set of data.

To characterize the resulting truncated beam profiles in terms of size and position, the first and second statistical moment, i.e., the weighted mean

$$\mu_z = \frac{1}{W}\sum_{i=1}^{N} z_i w_i, \tag{B4}$$

and the variance

$$\sigma_z^2 = \frac{1}{W}\sum_{i=1}^{N} (z_i - \mu_z)^2 w_i, \tag{B5}$$

where N is the number of used bins, z_i the position of the ith bin and w_i the corresponding signal, were calculated. The weight W is the sum of the individual weights w_i given by

$$W = \sum_{i=1}^{N} w_i. \tag{B6}$$

The procedure set forth above simplifies the comparison of the measured data to the simulation results.

APPENDIX C: OVERLAPPING OF TUNE-SPREAD WITH THE RESONANCE

In this section we derive the condition for the overlapping of the space charge tune-spread with a resonance of type $Q_x + 2Q_y = N$. We consider two characteristic points in the tune diagram: 1) the machine bare tunes Q_{x0}, Q_{y0}; 2) the depressed tunes $Q_{x1} = Q_{x0} + \Delta Q_{x,\max}, Q_{y1} = Q_{y0} + \Delta Q_{y,\max}$, i.e., the tunes of a particle experiencing the strongest space charge. According to our definition, the distance from the resonance of a particle with tunes Q_x, Q_y is $\Delta_r = Q_x + 2Q_y - N$. Specialized to the two characteristic points we find that the distance from the resonance of the bare tunes is $\Delta_{r0} = Q_{x0} + 2Q_{y0} - N$, and the distance from the resonance of the depressed tunes is $\Delta_{r1} = Q_{x1} + 2Q_{y1} - N$. It is straightforward to find that $\Delta_{r1} = \Delta_{r0} + \mathcal{D}_{\mathrm{r,sc}}$, with $\mathcal{D}_{\mathrm{r,sc}} = \Delta Q_{x,\max} + 2\Delta Q_{y,\max}$. The overlapping of the full tune-spread of the bunch with the resonance occurs when the following two conditions happen simultaneously: (1) (Q_{x0}, Q_{y0}) is above the resonance, namely when $0 \le \Delta_{r0}$; (2) (Q_{x1}, Q_{y1}) is below the resonance, namely when $\Delta_{r1} \le 0$, which implies $\Delta_{r0} + \mathcal{D}_{\mathrm{r,sc}} \le 0$. Both conditions (1) and (2) are satisfied only if

$$0 \le \Delta_{r0} \le -\mathcal{D}_{\mathrm{r,sc}}. \tag{C1}$$

This equation gives the condition for the overlapping of the space charge tune-spread with the resonance $Q_x + 2Q_y = N$. The quantity $\mathcal{D}_{\mathrm{r,sc}}$ naturally defines the width of the space charge tune-spread measured in the variable Δ_r, and it incorporates correctly the effect of both the space charge tune-shift $\Delta Q_{x,\max}$, and $\Delta Q_{y,\max}$ to discuss resonant phenomena created by the 4D coupled dynamics.

The space charge tune-spread becomes particularly important when we consider the resonance condition in an arbitrary longitudinal position z in a bunch. There we need to use the instantaneous depressed tunes associated to the freezing of the longitudinal motion. The maximum space charge detuning will now depend on z, hence we write $\Delta Q_{x,\max}(z)$, and $\Delta Q_{y,\max}(z)$. It becomes therefore natural to define $\mathcal{D}_{\mathrm{r,sc}}(z) = \Delta Q_{x,\max}(z) + 2\Delta Q_{y,\max}(z)$ (for our experiment $\mathcal{D}_{\mathrm{r,sc}}(0) = \mathcal{D}_{\mathrm{r,sc}} = -0.19$). By definition, for any particle with transverse amplitude X, Y located at z, $\Delta Q_{\mathrm{sc,x}}(X,Y) + 2\Delta Q_{\mathrm{sc,x}}(X,Y) \ge \mathcal{D}_{\mathrm{r,sc}}(z)$ is valid. Therefore, the distance from the resonance [Eq. (3)] for a particle at z can be lower bounded by $\Delta_r \ge \Delta_{r0} + \mathcal{D}_{\mathrm{r,sc}}(z)$. If $\Delta_{r0} + \mathcal{D}_{\mathrm{r,sc}}(z) > 0$, the resonance condition cannot be fulfilled by any particle having longitudinal position z.

[1] G. Franchetti, I. Hofmann, M. Giovannozzi, and M. Martini, and E. Métral, Space charge and octupole driven resonance trapping observed at the CERN Proton Synchrotron, Phys. Rev. ST Accel. Beams **6**, 124201 (2003).

[2] G. Franchetti, O. Chorniy, I. Hofmann, W. Bayer, F. Becker, P. Forck, T. Giacomini, M. Kirk, T. Mohite, C. Omet, A. Parfenova, and P. Schutt, Experiment on space charge driven nonlinear resonance crossing in an ion synchrotron, Phys. Rev. ST Accel. Beams **13**, 114203 (2010).

[3] P. Spiller and G. Franchetti, The FAIR accelerator project at GSI, Nucl. Instrum. Methods Phys. Res., Sect. A **561**, 305 (2006).

[4] J. Coupard *et al.*, LIU Technical Design Report (TDR), Report No. CERN-ACC-2014-0337.

[5] O. Bruning *et al.*, Report No. CERN-2004-003, 2004.

[6] *Proceedings of all HB workshops*.

[7] R. Baartman, Betatron resonances with space charge, AIP Conf. Proc. **448**, pp. 56 (1998).

[8] I. Hofmann, Stability of anisotropic beams with space charge, Phys. Rev. E **57**, 4713 (1998).
[9] M. Venturini and R. L. Gluckstern, Resonance analysis for a space charge dominated beam in a circular lattice, Phys. Rev. ST Accel. Beams **3**, 034203 (2000).
[10] I. Hofmann, G. Franchetti, J. Qiang, and R. Ryne, Self-consistency and coherent effects in nonlinear resonances, AIP Conf. Proc. **693**, 65 (2003).
[11] S. Y. Lee, Fundamental Limit of Nonscaling Fixed-Field Alternating-Gradient Accelerators, Phys. Rev. Lett. **97**, 104801 (2006).
[12] S. Y. Lee, G. Franchetti, I. Hofmann, F. Wang, and L. Yang, Emittance growth mechanisms for space-charge dominated beams in fixed field alternating gradient and proton driver rings, New J. Phys. **8**, 291 (2006).
[13] G. Franchetti and F. Schmidt, Extending the Nonlinear-Beam-Dynamics Concept of 1D Fixed Points to 2D Fixed Lines, Phys. Rev. Lett. **114**, 234801 (2015).
[14] G. Franchetti and F. Schmidt, http://arxiv.org/abs/1504.04389.
[15] E. Todesco, Analysis of resonant structures of four-dimensional symplectic mappings, using normal forms, Phys. Rev. E **50**, R4298 (1994).
[16] M. Gemmi and E. Todesco, Stability and geometry of third-order resonances in four-dimensional symplectic mappings, Celest. Mech. Dyn. Astron. **67**, 181 (1997).
[17] R. Hagedorn, Report No. CERN 57–1, 1957.
[18] R. Hagedorn and A. Schoch, Report No. CERN 57–14, 1957.
[19] A. Schoch, Report No. CERN 57-23, 1958.
[20] G. Guignard, Report No. CERN 76–06, 1976.
[21] G. Guignard, Report No. CERN 78–11, 1978.
[22] M. N. Vrahatis, H. Isliker, and T. C. Bountis, Structure and breakdown of invariant tori in a 4-D mapping model of accelerator dynamics, Int. J. Bifurcation Chaos Appl. Sci. Eng. **07**, 2707 (1997).
[23] A. Huschauer, M.S. thesis, CERN Report No. CERN-THESIS-2012-212, TU Wien, 2012, http://cds.cern.ch/record/1501943/.
[24] M. Gasior, Report No. CERN LHC-Project-Report-853, 2000.
[25] H. Burkhardt, G. Rumolo, and F. Zimmermann, in *Proceedings of the 2003 Particle Accelerator Conference, Portland, OR* (IEEE, New York, 2003), p. 3041.
[26] Ch. Steinbach, Report No. CERN-PS-95-04-OP, 1995.
[27] D. Belohrad, Ph.D. thesis, Czech Technical University in Prague, 2010; Report No. CERN-Thesis-2010-131.
[28] S. Hancock, M. Lindroos, and S. Koscielniak, Longitudinal phase space tomography with space charge, Phys. Rev. ST Accel. Beams **3**, 124202 (2000).
[29] V. Kapin and Y. Alexahin, in *Proceedings of RuPAC-2010* (Protvino, Russia, 2010), paper WEPSB017.
[30] G. Franchetti and I. Hofmann, Particle trapping by nonlinear resonances and space charge, Nucl. Instrum. Methods Phys. Res., Sect. A **561**, 195 (2006).
[31] A. G. Ruggiero, Report No. FERMILAB-FN-0258, 1974.
[32] S. Gilardoni and D. Manglunki, Report No. CERN-2011-004, 2011, http://cds.cern.ch/record/1359959.
[33] M. Juchno, Ph.D. thesis, EPFL, Lausanne, 2013.
[34] M. Giovannozzi, *Proceedings of the PTC 1/2 day*, (CERN, Geneva, Switzerland, 2011), https://indico.cern.ch/event/162516/.